A segregated spectral finite element method for the 2D transient incompressible Navier–Stokes equations

Wenqiang He, Guoliang Qin *, Jingxiang Lin, Cheng Jia

School of Energy and Power Engineering, Xi'an Jiaotong University, Xi'an 710049, China

ARTICLE INFO

ABSTRACT

In this paper, the spectral element approximation and the velocity–pressure decoupling method implementing the SIMPLE (semi-implicit method for pressure linked equations) algorithm are first combined to form a high-order segregated scheme for the solution of the two-dimensional transient incompressible Navier–Stokes equations. In contrast to previous segregated finite element methods based on the SIMPLE algorithm, the pressure equation is derived from the continuity equation using the element matrices to ensure convergence. High-order element basis functions are adopted, which greatly reduces the number of nodal points used in the calculation. The validation test that has an analytical solution demonstrates the high accuracy and convergence rate of the method. The flow in a lid-driven cavity with different inclination angles and the flow over a backward-facing step are investigated to further illustrate the performance of the scheme. The computed results are in excellent agreement with the benchmark solutions. The almost periodic solution for the flow of Re=10000 in a lid-driven square cavity is also captured by the present scheme.

© 2019 Elsevier Ltd. All rights reserved.

1. Introduction

The application of the Navier–Stokes equations (NSE) to solve fluid flow has received much attention during the last decades. Numerous numerical schemes have been used for the solution of the NSE. For incompressible flow, one of the major difficulties encountered in constructing the numerical schemes arises from the implicit coupling of the velocity and pressure through the continuity equation, which has a non-evolutionary characteristic preventing the straightforward integration of the equation in time.

The pressure-correction scheme that belongs to the family of segregated algorithms is one of the most commonly used techniques for an efficient solution of the NSE. The velocity components and pressure are solved separately and the computational effort is greatly reduced. The SIMPLE algorithm of Patankar and Spalding [1] is a formulation that has been widely applied to flow problems. As analysed by Tao [2], the final solution will not be affected by the two major assumptions in the SIMPLE algorithm if the iterative process converges. However, the convergence rate and stability will certainly be affected. Many variants have been produced to improve the convergence rate of the scheme. Patankar [3] proposed the SIMPLER algorithm to overcome the inconsistency between the initial velocity field and the initial pressure field. Van Doormaal and Raithby [4] presented the SIMPLEC algorithm to partially compensate for the effect of neglecting the velocities of neighbouring nodes by redefining the coefficients of the velocity correction equation. Qu et al. [5] provided the CLEAR algorithm to address the two assumptions in the SIMPLE algorithm by re-solving the pressure field

---

* Corresponding author.
  E-mail address: glqin@mail.xjtu.edu.cn (G. Qin).

Nomenclature

E_x	Number of elements along x axis
E_y	Number of elements along y axis
L	Width of the square, m
L_0	Characteristic length
N_x	Interpolation order along x axis
N_y	Interpolation order along y axis
N_e	Number of elements
N_d	Number of nodal points in standard element
N_G	Total number of nodal points
p	Dimensionless pressure *Superscripts*
P	Projector onto the divergence-free subspace
Re	Reynolds number $[= u_0 L_0 / \mu]$
S	Height of the backward step
t	Dimensionless time
T	Computational time
$\boldsymbol{u}$	Velocity vector $(= u, v)$
u, v	Dimensionless velocity components
u_0	Characteristic velocity
x, y	Dimensionless Cartesian coordinates

Greek symbols

α_p	Pressure relaxation factor
α_u	Velocity relaxation factor
Γ	Boundary of computational domain
ξ, η	Reference coordinates
θ	Cavity inclination angle
μ	Kinematic viscosity, m^2/s
ν	Reciprocal of Reynolds number
Ω	Computational domain

Superscripts

D	Diagonal elements of a matrix
e	Element symbol
k	Iterative step
n	Time step
O	Off-diagonal elements of a matrix
$*$	Intermediate value

Subscripts

,	Spatial derivative

based on the intermediate velocity. Sun et al. [6,7] developed the IDEAL algorithm to further enhance the robustness and convergence rate of the CLEAR algorithm by double inner iterative processes for the pressure equation. Considering the successful application of the SIMPLE algorithm in the finite difference and finite volume schemes, finite element methods (FEM) taking advantages of the SIMPLE algorithm or its variant has also been presented. Rice and Schnipke [8] introduced a SIMPLE-like segregated velocity–pressure method employing the streamline upwind scheme. Van Zijl and Du Toit [9] implemented the SIMPLEST algorithm to the streamline upwind/Petrov–Galerkin (SUPG) FEM to generate symmetric coefficient matrices associated with the momentum equations. Du Toit [10] investigated the application of the SIMPLER and SIMPLEST algorithms to the non-conservative form of the NSE along with consistent and inconsistent SUPG weightings. Malatip et al. [11] combined the segregated algorithm used by Rice and Schnipke [8] and the SUPG method for the solution of conjugate heat transfer problems.

Although the SIMPLE algorithm has been widely used in different numerical methods, the combination of the SIMPLE algorithm and high-order schemes especially in combination with spectral interpolation functions, has been investigated in only a few studies. A spectral element method (SEM) proposed by Patera [12] combines the flexibility of FEM and

the high accuracy of the spectral method. Opposed to the usual FEM approach, infinite-order orthogonal polynomials are used by the SEM to construct the interpolants instead of using low-order algebraic polynomials in each element. Therefore, exponential convergence can be obtained for a problem with a solution that is sufficiently smooth. Xu and Lin [13] adopted the spectral element approximation for the solution of the NSE, employing the classical Uzawa algorithm to decouple the global discrete saddle point problem. Kim and Beskok [14] combined the SEM and the algebraic factorization method for incompressible flow and heat transfer problems, which has a great advantage because no artificial boundary condition is needed for the pressure equation. Ranjan et al. [15] used the stabilized SEM based on the SUPG formulation to solve the two-dimensional transient NSE, in which two kinds of preconditioners are employed to speed up the solution process. Hsu et al. [16] investigated the flow patterns past two staggered arrays of cylinders using the SEM and a time-splitting scheme, which is more efficient than the Uzawa algorithm. Despite the fact that the SEM for incompressible flow has been studied by many researchers [17–22], there seems to be no attempt presented in the literature to combine the SEM and the mature SIMPLE algorithm to build an efficient high-order scheme.

The aim of this paper is to combine the high accuracy and flexibility of SEM in spatial discretization and the advantage of the SIMPLE algorithm in decoupling the velocity and pressure to form an efficient high-order numerical scheme for the solution of incompressible flow. A problem with an analytical solution is firstly considered. Then the flow in a lid-driven cavity with different inclination angles is solved and the computed results are compared with benchmark solutions. The flow over a backward-facing step is also simulated. Numerical experiments show that the segregated SEM is efficient and accurate, and that the results of the flow in a lid-driven cavity can be used as reference solutions. It is believed that the proposed method can promote the further application of high-order algorithms for the solution of incompressible flow and heat transfer problems.

2. Governing equations and mathematical formulation

2.1. Governing equations

Let Ω be a two-dimensional regular and bounded domain with boundary Γ. The non-dimensional NSE used to describe transient incompressible flow in tensor notation can be written as

$$u_{i,i} = 0, \text{ in } \Omega \times [0, T] \tag{1}$$

$$\frac{\partial u_i}{\partial t} + u_j u_{i,j} + p_{,i} - \nu u_{i,jj} = f_i, \text{ in } \Omega \times [0, T] \tag{2}$$

with $i, j = 1, 2$. Here $[0, T]$ represents the temporal domain, and u_i, p, f_i, t, ν are the velocity components, pressure, external forces, time and the reciprocal of the Reynolds number, respectively. The subscript ',' denotes the spatial derivative, e.g., $u_{i,j}$ represents the derivative of u_i with respect to j direction.

The boundary conditions for Eqs. (1) and (2) can be expressed as follows

$$u_i = g_i, \text{ on } \Gamma_g \tag{3}$$

$$(-p\delta_{ij} + \nu u_{i,j})n_j = h_i \text{ on } \Gamma_h \tag{4}$$

where Γ_g and Γ_h are two disjoint subsets of Γ, g_i is the velocity vector prescribed on Γ_g, h_i is the traction vector prescribed on Γ_h, n_j is the jth component of the unit vector normal to Γ_h. The initial conditions for Eqs. (1) and (2) are

$$u_i(0, \boldsymbol{x}) = u_{i0}(\boldsymbol{x}) \tag{5}$$

2.2. Spectral element discretization of the momentum equation

After multiplying the momentum equation by the velocity test function and integrating over the computational domain Ω, the Galerkin variational problem is to find $(u_i, p) \in H_0^1(\Omega) \times L^2(\Omega)$ such that

$$
\begin{aligned}
&\int_{\Omega} [(\frac{\partial u_i}{\partial t} + u_j u_{i,j})\delta u_i - p\delta u_{i,i} + \nu u_{i,j}\delta u_{i,j}]d\Omega \\
&= \int_{\Omega} f_i \delta u_i d\Omega + \int_{\Gamma_h} h_i \delta u_i d\Gamma \qquad \forall \delta u_i \in H^1(\Omega)
\end{aligned}
\tag{6}
$$

where δu_i is the velocity test function, $L^2(\Omega)$ denotes the space of square-integrable functions, $H_0^1(\Omega)$ denotes the space of vector functions whose components and their first derivatives are square-integrable and vanish on $\partial\Omega$.

Similar to the usual FEM approach, the computational domain is first discretized into N_e non-overlapping elements $\Omega = \sum_{i=1}^{N_e} \Omega^e$ as illustrated in Fig. 1. Quadrilateral elements will be employed in the simulation. E_x and E_y are the number of elements in x- and y-directions. Let φ be the mapping from the physical coordinate (x, y) to the computational coordinate (ξ, η), then the actual element Ω^e can be transformed into the standard element $\Omega^{st} = [-1, 1] \times [-1, 1]$ as
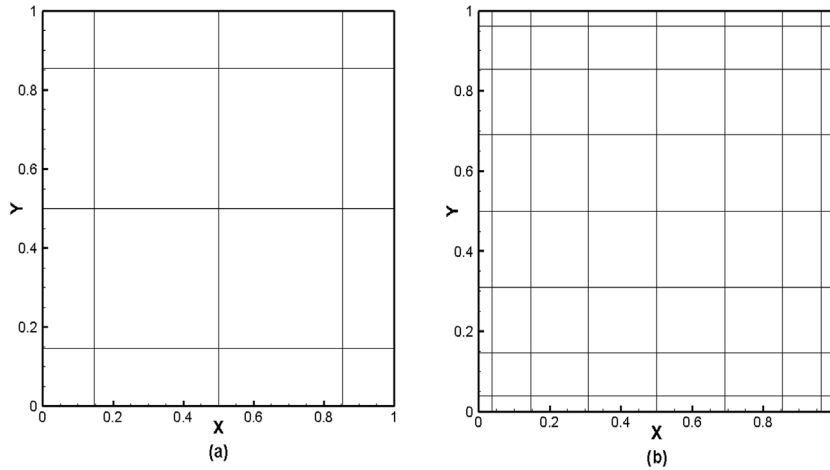
Fig. 1. Distribution of rectangular elements in the computational domain (a) $E_x = E_y = 4$ (b) $E_x = E_y = 8$.
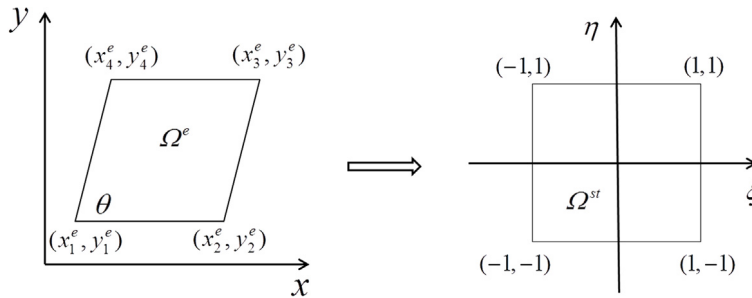

Fig. 2. Transformation from actual element to standard element.

shown in Fig. 2. For the quadrilateral element with parallel walls at different inclinations, the transformation relationship can be expressed as

$$
\begin{pmatrix} \xi \\ \eta \end{pmatrix} = \begin{pmatrix} \dfrac{2}{L_x^e} & -\dfrac{2}{L_x^e}\dfrac{\cos(\theta)}{\sin(\theta)} \\ 0 & \dfrac{2}{L_y^e} \end{pmatrix} \begin{pmatrix} x - \dfrac{x_3^e + x_1^e}{2} \\ y - \dfrac{y_2^e + y_1^e}{2} \end{pmatrix}
\tag{7}
$$

Here $L_x^e = x_2^e - x_1^e$ and $L_y^e = y_3^e - y_1^e$ in Eq. (7). In the standard element, the LGL (Legendre–Gauss–Lobatto) points of degree N_x and N_y in x- and y-directions are chosen as interpolation nodes as presented in Fig. 3 and equal-order interpolation is used for both the velocity and pressure.

Thus according to the spectral approximation theory, u_i and p along with the test functions δu_i and δp can be written as

$$
u_i = \sum_{J=1}^{N_d} u_{iJ}\Phi_J, \quad \delta u_i = \sum_{I=1}^{N_d} \Phi_I
\tag{8}
$$

$$
p = \sum_{J=1}^{N_d} p_J\Phi_J, \quad \delta p = \sum_{I=1}^{N_d} \Phi_I
\tag{9}
$$

where N_d is the number of nodes in the standard element, Φ_I, Φ_J are the nodal basis functions at node I and J, and u_{iJ}, p_J are the values of u_i and p at node J.

The nodal basis function has the form

$$
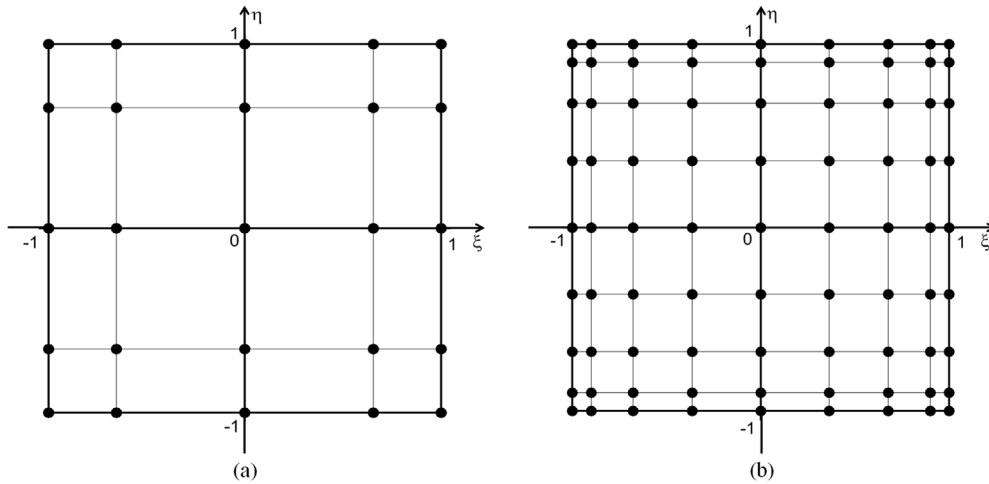\Phi_I = \sum_{j=0}^{N_x} \sum_{k=0}^{N_y} \phi_j(\xi)\phi_k(\eta)
\tag{10}
$$

Fig. 3. Distribution of LGL nodes in the standard element (a) $N_x = N_y = 4$ (b) $N_x = N_y = 8$.

$$\phi_j(\xi) = \sum_{m=0}^{N_x} \frac{1}{\gamma_m} L_m(\xi_j) L_m(\xi) \omega_j \tag{11}$$

$$\phi_k(\eta) = \sum_{n=0}^{N_y} \frac{1}{\gamma_n} L_n(\eta_k) L_n(\eta) \omega_k \tag{12}$$

where L_m, L_n are the Legendre polynomials. The functions $\phi_j(\xi)$, $\phi_k(\eta)$ are equal to zero outside the standard element. And γ_m, ω_j are expressed as

$$\gamma_m = \begin{cases} \dfrac{1}{m+0.5} & m < N_x \\ \dfrac{2}{N_x} & m = N_x \end{cases} \tag{13}$$

$$\omega_j = \frac{2}{N_x(N_x+1)} \frac{1}{[L_{N_x}(x_j)]^2} \quad j = 0, \ldots, N_x \tag{14}$$

In each element, substitute the interpolants of the different variables into Eq. (6). We note here that the equations are not discretized over the whole computational domain, only the interpolants involve the discrete values associated with the nodal points. The resulting element formulation of the momentum equation yields

$$\mathbf{M}_{IJ}^e \frac{\mathrm{d}u_{ij}^e}{\mathrm{d}t} + \mathbf{C}_{IJ}^e u_{ij}^e + \nu \mathbf{D}_{IJ}^e u_{ij}^e - \mathbf{G}_{iIJ}^e p_j^e = \mathbf{M}_{IJ}^e f_{ij}^e + \mathbf{F}_{IJ}^e h_{ij}^e \tag{15}$$

where $\mathbf{M}_{IJ}^e$, $\mathbf{C}_{IJ}^e$, $\mathbf{D}_{IJ}^e$, $\mathbf{G}_{iIJ}^e$ and $\mathbf{F}_{IJ}^e$ are defined as

$$\mathbf{M}_{IJ}^e = \int_{\Omega^e} \Phi_J \Phi_I \mathrm{d}\Omega \tag{16}$$

$$\mathbf{C}_{IJ}^e = \int_{\Omega^e} u_{iK}^{n+1,k} \Phi_K \Phi_{J,i} \Phi_I \mathrm{d}\Omega \tag{17}$$

$$\mathbf{G}_{iIJ}^e = \int_{\Omega^e} \Phi_J \Phi_{I,i} \mathrm{d}\Omega \tag{18}$$

$$\mathbf{D}_{IJ}^e = \int_{\Omega^e} \Phi_{J,i} \Phi_{I,i} \mathrm{d}\Omega \tag{19}$$

$$\mathbf{F}_{IJ}^e = \int_{\Gamma} \Phi_J \Phi_I \mathrm{d}\Gamma \tag{20}$$

where subscripts 'I', 'J', 'K' are the node indices, 'i' is the spatial index, $u_i^{n+1,k}$ is the kth iterative velocity of the $(n+1)$th time step. For the sake of simplicity, the time step superscript of intermediate values in the iterative process will be omitted in the following part of the paper. It can be seen that only the element matrix of the convective term $\mathbf{C}_{IJ}^e$ needs to be updated repeatedly during the iteration of each time step.

2.3. Segregated method based on the SIMPLE algorithm

2.3.1. Momentum equation

As in the SIMPLE algorithm, the equation coefficients and source terms of the $(k + 1)$th iterative step are based on the velocity u_i^k. The non-diagonal contributions of the element coefficient matrix of the convective term are treated explicitly in order to keep the left matrix symmetric. This method is the so-called SIMPLEST formulation that has been employed in [9,10]. Eq. (15) is integrated using an implicit backward difference scheme with time step Δt. Accordingly, the momentum equation for the intermediate velocity u_i^* corresponding to the pressure p^k in the element matrix form is expressed as

$$
\mathbf{M}_{IJ}^e \frac{\beta_0 u_{iJ}^{e,*} - \sum_{j=1}^m \beta_j u_{iJ}^{e,n+1-j}}{\Delta t} + \mathbf{C}_{IJ}^{e,D} u_{iJ}^{e,*} + \nu \mathbf{D}_{IJ}^e u_{iJ}^{e,*} - \mathbf{G}_{iIJ}^e p_J^{e,k}
$$
$$
= \mathbf{M}_{IJ}^e f_{iJ}^{e,n+1} - \mathbf{C}_{IJ}^{e,O} u_{iJ}^{e,k} + \mathbf{F}_{IJ}^e h_{iJ}^{e,n+1}
\tag{21}
$$

where $\mathbf{C}^{e,D}$ and $\mathbf{C}^{e,O}$ are the diagonal and non-diagonal matrices of $\mathbf{C}^e$, respectively. For a second-order backward difference scheme the formulation is given as

$$
\frac{3}{2\Delta t} \mathbf{M}_{IJ}^e u_{iJ}^{e,*} + \mathbf{C}_{IJ}^{e,D} u_{iJ}^{e,*} + \nu \mathbf{D}_{IJ}^e u_{iJ}^{e,*} = \mathbf{G}_{iIJ}^e p_J^{e,k} - \mathbf{C}_{IJ}^{e,O} u_{iJ}^{e,k}
$$
$$
+ \mathbf{M}_{IJ}^e (\frac{2}{\Delta t} u_{iJ}^{e,n} - \frac{1}{2\Delta t} u_{iJ}^{e,n-1} + f_{iJ}^{e,n+1}) + \mathbf{F}_{IJ}^e h_{iJ}^{e,n+1}
\tag{22}
$$

To address large velocity changes between successive iterations, velocity under-relaxation is incorporated into the solution of the equation with α_u the relaxation factor. Then Eq. (22) can be rewritten as

$$
(\mathbf{S}_{IJ}^{e,D} + \alpha_u \mathbf{S}_{IJ}^{e,O}) u_{iJ}^{e,*} = \alpha_u \mathbf{G}_{iIJ}^e p_J^{e,k} + c_{iI}^e
\tag{23}
$$

where

$$
\mathbf{S}_{IJ}^{e,D} = \frac{3}{2\Delta t} \mathbf{M}_{IJ}^{e,D} + \mathbf{C}_{IJ}^{e,D} + \nu \mathbf{D}_{IJ}^{e,D}
$$
$$
\mathbf{S}_{IJ}^{e,O} = \frac{3}{2\Delta t} \mathbf{M}_{IJ}^{e,O} + \nu \mathbf{D}_{IJ}^{e,O}
\tag{24}
$$

$$
c_{iI}^e = \alpha_u [-\mathbf{C}_{IJ}^{e,O} u_{iJ}^{e,k} + \mathbf{M}_{IJ}^e (\frac{2}{\Delta t} u_{iJ}^{e,n} - \frac{1}{2\Delta t} u_{iJ}^{e,n-1} + f_{iJ}^{e,n+1})
$$
$$
+ \mathbf{F}_{IJ}^e h_{iJ}^{e,n+1}] + (1 - \alpha_u) \mathbf{S}_{IJ}^{e,D} u_{iJ}^{e,k}
\tag{25}
$$

$\mathbf{S}^{e,D}$ and $\mathbf{S}^{e,O}$ are the diagonal and non-diagonal matrices of $\mathbf{S}^e$, respectively. Assembling the element matrices in the conventional manner, the global matrix form of Eq. (23) is formulated as

$$
(\mathbf{S}_{IJ}^D + \alpha_u \mathbf{S}_{IJ}^O) u_{iJ}^* = \alpha_u \mathbf{G}_{iIJ} p_J^k + c_{iI}
\tag{26}
$$

where $\mathbf{S}^D$, $\mathbf{S}^O$, $\mathbf{G}_i$ and c_i are the global matrices and the global vector, respectively.

2.3.2. Pressure equation

The discrete momentum equation (23) can be rearranged to give

$$
u_{iI}^{e,k+1} = \hat{u}_{iI}^e + q_{iI}^{e,*}
\tag{27}
$$

where

$$
\hat{u}_{iI}^e = (\mathbf{S}_{IK}^{e,D})^{-1} (-\alpha_u \mathbf{S}_{KJ}^{e,O} u_{iJ}^{e,*} + c_{iI}^e)
\tag{28}
$$
$$
q_{iI}^{e,*} = \mathbf{R}_{iIJ}^e p_J^{e,*} = \alpha_u (\mathbf{S}_{IK}^{e,D})^{-1} \mathbf{G}_{iKJ}^e p_J^{e,*}
\tag{29}
$$

Due to the diagonal nature of $\mathbf{S}^{e,D}$, its inverse form $(\mathbf{S}^{e,D})^{-1}$ is very simple to calculate. The weak formulation of the continuity equation is obtained by multiplying the pressure test function δp and applying the divergence theorem, and it is written as

$$
\int_\Omega u_i^{k+1} \delta p_{,i} d\Omega = \int_\Gamma g_i^{n+1} \delta p n_i d\Gamma
\tag{30}
$$

It can be seen that the velocity flux on the boundary is employed as the pressure boundary condition, hence no artificial pressure boundary condition needs to be constructed. Substituting Eq. (27) into the weak formulation of the continuity equation and using the interpolants of the variables, the continuity equation in element matrix form can be expressed as

$$
\mathbf{G}_{iIJ}^e q_{iJ}^{e,*} = -\mathbf{G}_{iIJ}^e \hat{u}_{iJ}^e + \mathbf{F}_{IJ}^e g_{iJ}^{e,n+1} n_i
\tag{31}
$$

Assembling the element matrices in Eqs. (29) and (31) into global ones, they have the form

$$\mathbf{G}_{ilJ} q_{iJ}^* = -\mathbf{G}_{ilJ} \hat{u}_{iJ} + \mathbf{F}_{IJ} g_{ij}^{n+1} n_i \tag{32}$$

$$q_i^* = \mathbf{R}_{ilJ} p_J^* \tag{33}$$

where $\mathbf{G}_i$, $\mathbf{R}_i$ and $\mathbf{F}$ are the global matrices. Then the pressure equation is obtained from Eqs. (32) and (33), and can be written as

$$\mathbf{H}_{IJ} p_J^* = -\mathbf{G}_{ilJ} \hat{u}_{iJ} + \mathbf{F}_{IJ} g_{ij}^{n+1} n_i \tag{34}$$

where

$$\mathbf{H}_{IJ} = \mathbf{G}_{ilK} \mathbf{R}_{iKJ} = \alpha_u \mathbf{G}_{ilK} (\mathbf{S}_{KL}^D)^{-1} \mathbf{G}_{ilJ} \tag{35}$$

Compared to the usual FEM, the pressure equation is derived from the element matrices, which involves no pressure assumption. It was found that the pressure gradient assumption adopted in the FEM [8] introduces deviations into the initial iterative process of the pressure equation. For the low-order FEM, the initial perturbations will gradually decrease with the iterative process until it completely disappears. However, the high-order SEM is very sensitive to the initial perturbations, which will be continuously amplified so that no converged pressure solution can be obtained. Therefore, the method to derive the pressure equation adopted in this paper ensures the advancement of the iterative process. The global matrix $\mathbf{G}_i$ can be preprocessed once before the iterative procedure and the matrix $\mathbf{S}^D$ have been calculated whilst solving the momentum equation, therefore the computational effort for the pressure equation is greatly reduced.

To restrict the pressure change between two successive iterations, the pressure should also be relaxed to get converged solutions, the under-relaxation form is expressed as

$$p^{k+1} = \alpha_p p^* + (1 - \alpha_p) p^k \tag{36}$$

where α_p is the pressure relaxation factor. Once the pressure is calculated, the velocity components are updated by the newly obtained values to ensure continuity during each iteration, the velocity correction is given as

$$u_{il}^{k+1} = \hat{u}_{il} + \alpha_u (\mathbf{S}_{IK}^D)^{-1} \mathbf{G}_{iKJ} p_J^{k+1} \tag{37}$$

From the above process, it can be seen that the decoupling of the velocity and pressure for each iteration in a time step of the SIMPLE algorithm is very similar to that in the projection method [23]. Taking advantage of the analytical techniques in [24], we briefly illustrate that the decoupling scheme adopted in this paper is stable (see Appendix).

3. Computational procedure

The iterative process is repeated until the converged numerical solutions of the $(n + 1)$th time step are obtained. The steps of the segregated algorithm in a single time step are illustrated as follows

1. Guess the initial velocity field and the initial pressure field
2. Calculate the coefficients and source terms for the intermediate velocity u_i^*
3. Solve the momentum equation (26) to obtain u_i^* and rearrange Eq. (23) to get $\hat{u}_i^e$ and $q_i^{e,*}$.
4. Take advantage of the element matrices to construct the pressure equation and get the new pressure value p^{k+1}.
5. Use Eq. (37) to update the velocity u_i^{k+1}, and ensure continuity by the newly obtained pressure.
6. Go to step 2 and repeat the calculation until the converged solutions of a time step are obtained

4. Numerical results and discussions

4.1. Scheme validation with analytical solution

A test problem with an analytical solution is simulated in order to validate the SEM code and illustrate its performance, numerical accuracy and convergence rate. The analytical solution has the form

$$\begin{aligned}
u &= \sin(\pi x) \sin(\pi y) \arctan(2\pi^2 t) \\
v &= \cos(\pi x) \cos(\pi y) \arctan(2\pi^2 t) \\
p &= \sin(x - y) \arctan(2\pi^2 t)
\end{aligned} \tag{38}$$

on the computational domain of $\Omega = \{(x, y): 0 \le x \le 1, 0 \le y \le 1\}$. The initial conditions, boundary conditions and source terms can be deduced from Eq. (38). The L_2 and L_∞ norms of the error are employed to evaluate the numerical accuracy, and they are depicted as

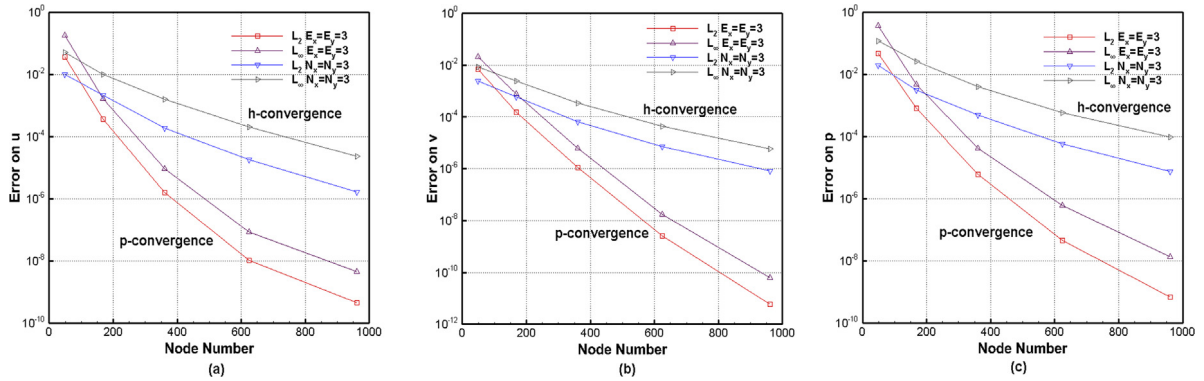$$\|\zeta\| = \left[\frac{1}{N_G} \sum_{j=1}^{N_G} (\zeta_j^{num} - \zeta_j^{ana})^2\right]^{1/2} \tag{39}$$

Fig. 4. The *p*-convergence and *h*-convergence rates of (a) *u*-velocity, (b) *v*-velocity and (c) pressure in L_2 and L_∞ norms.
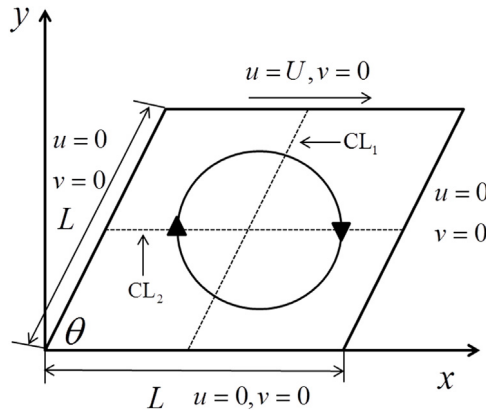

Fig. 5. Schematic and boundary conditions for the flow in a lid-driven cavity.

$$\|\zeta\|_\infty = \max_{j=1,\ldots,N_G} \left|\zeta_j^{num} - \zeta_j^{ana}\right| \tag{40}$$

where superscript "*num*" and "*ana*" represent the numerical and analytical results, ζ denotes the variables u_i and p, j is the node number and N_G is the total number of nodal points.

The studies of *p*-convergence and *h*-convergence are performed for the analytical problem. In the *p*-convergence study, the spatial discretization is fixed ($E_x = E_y = 3$) and the polynomial orders of the element basis function ($N_x = N_y$) are systematically increased. Whilst in the *h*-convergence study, the polynomial orders are fixed ($N_x = N_y = 3$) and the element numbers in *x*- and *y*-directions ($E_x = E_y$) are gradually increased. For $\nu = 1.0$, the time step is set to be $\Delta t = 0.0001$, which is very small to avoid any temporal error. The under-relaxation factors for the velocity and pressure are $\alpha_u = \alpha_p = 1.0$. The test problem is simulated until $T = 1.0$ and the results are presented in Fig. 4. Both the L_2 and L_∞ norms of the error verify the validity of our method, and that a high accuracy can be obtained by increasing the polynomial orders or element numbers. Meanwhile, the *p*-convergence shows higher accuracy and faster convergence relative to the *h*-convergence, which illustrates the advantages of the high-order element basis functions adopted in the segregated SEM.

4.2. Flow in a lid-driven cavity

In this section, the segregated SEM is applied to the flow in a lid-driven cavity with different inclination angles to further evaluate its validity and numerical accuracy. The geometry and boundary conditions of this problem are presented in Fig. 5. Although the physical model is uncomplicated, it contains rich fluid flow phenomena and multiple counter-rotating recirculating regions. Therefore this problem has been presented by many researchers [25–30] in the literature as a benchmark problem for the evaluation of numerical schemes.

The Reynolds number is defined as $Re = {}^{UL}/_\mu$, where the characteristic velocity u_0 is equal to U, the characteristic length L_0 is equal L and μ is the kinematic viscosity. The time step for all the computations of the flow in a lid-driven cavity is set to be $\Delta t = 0.01$, the under-relaxation factors are $\alpha_u = 0.7$ and $\alpha_p = 0.2$. In order to test the grid independence, three different element divisions (6×6, 8×8 and 10×10) with an eighth-order polynomial in each element are adopted.

Table 1
Grid independence test of u-velocity on centreline CL_1 in a square cavity.

y	49×49	65×65	81×81
0.9688	0.5731	0.5800	0.5802
0.9531	0.4624	0.4711	0.4712
0.7344	0.1716	0.1877	0.1878
0.5000	−0.0551	−0.0618	−0.0618
0.2813	−0.2883	−0.2792	−0.2792
0.1016	−0.3025	−0.2993	−0.2995
0.0625	−0.1926	−0.2015	−0.2016

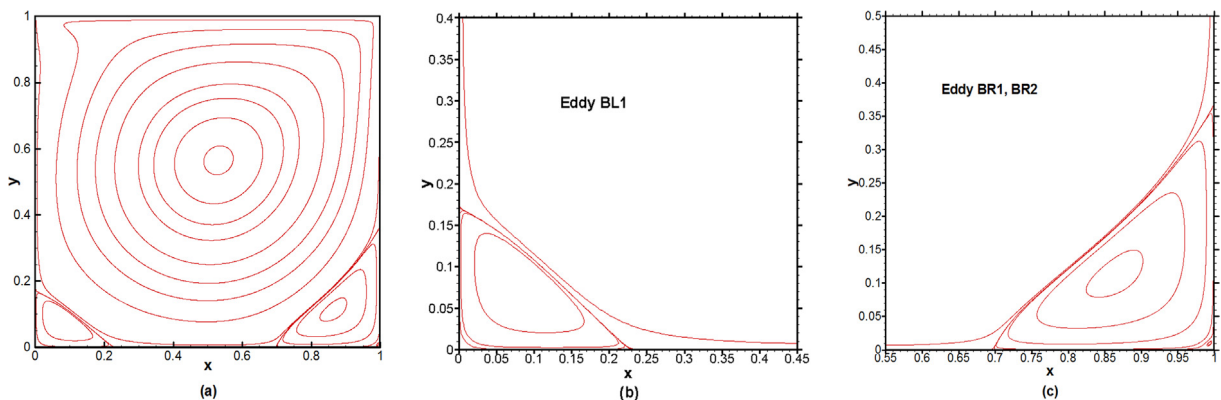**Fig. 6.** Nonuniform grid used for the flow in a lid-driven inclined cavity with $\theta = \pi/4$.

Fig. 7. Streamline contours and additional corner vortices in a square cavity for $Re = 1000$.

Numerical experiments using the three nonuniform grids of 49×49, 65×65 and 81×81 are performed for the flow of $Re = 1000$ in a square cavity. The u-velocities on the centre-line CL_1 are tabulated in Table 1, which show that the grid of 65×65 is sufficient to compute the flow. The nonuniform grid of 65×65 for the inclined cavity with $\theta = \pi/4$ is presented in Fig. 6.

4.2.1. Results for the flow in a square cavity

Figs. 7 and 8 show the steady streamline contours in a square cavity for $Re = 1000$ and 7500, respectively. The counter-rotating secondary vortices that develop with the increase of the Reynolds number in the corners are depicted by the streamline patterns. It can also be seen from Fig. 7 that there is a tertiary vortex in the lower right corner for $Re = 1000$, which is usually not captured by the low-order algorithms on such a coarse grid. This demonstrates the advantage of SEM as a high-order scheme to efficiently resolve the details of the flow. For the flow of $Re = 7500$, a counter-rotating secondary vortex appears in the upper left corner. Local magnifications of the corners are also included in Figs. 7 and 8 to better illustrate the secondary and tertiary vortices of the flow. The abbreviations BL, BR and TL represent the bottom left, bottom right and top left corners of the square cavity, respectively. Table 2 compares the location data of the primary, secondary and tertiary vortices for $Re = 1000$ and 7500 with the benchmark results [25,27]. It can be seen that the present vortex locations are in excellent agreement with the corresponding reference locations.

Figs. 9 and 10 show the velocity profiles on the centrelines CL_1 and CL_2 for $Re = 1000$ and 7500, respectively. These profiles show that the results compare very well with the reference solutions, especially those that Erturk et al. [27] produced on a high quality grid of 601×601. Tables 3 and 4 tabulate the percentage deviations of the results for Re
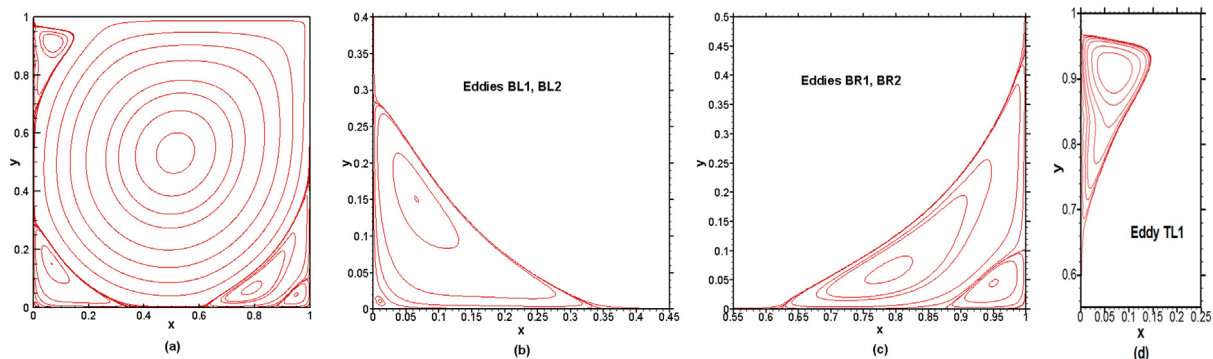
Fig. 8. Streamline contours and additional corner vortices in a square cavity for $Re = 7500$.
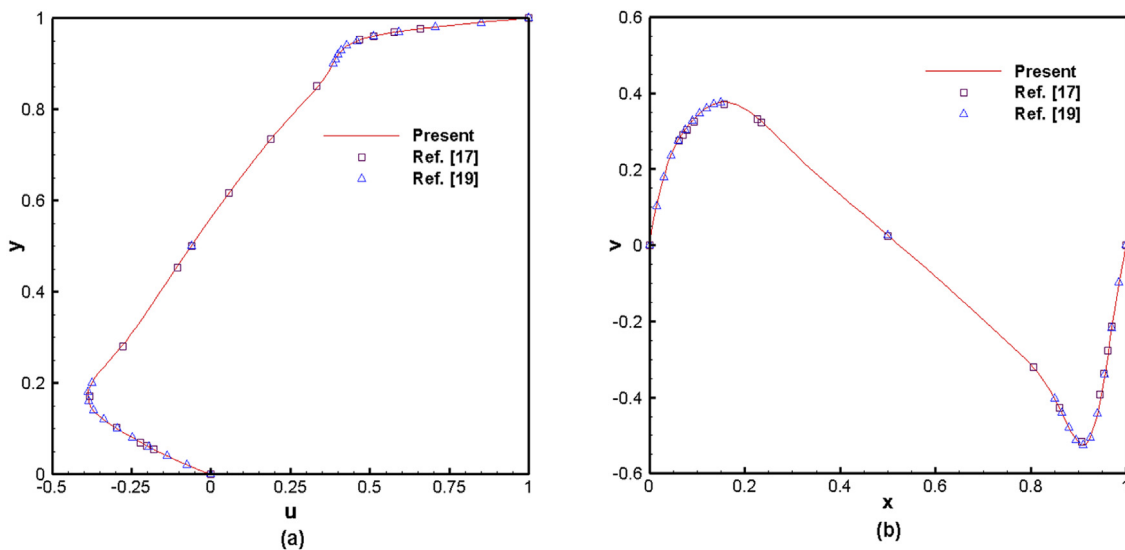

Fig. 9. (a) u-velocity profile on centreline CL_1 and (b) v-velocity profile on centreline CL_2 in a square cavity for $Re = 1000$.
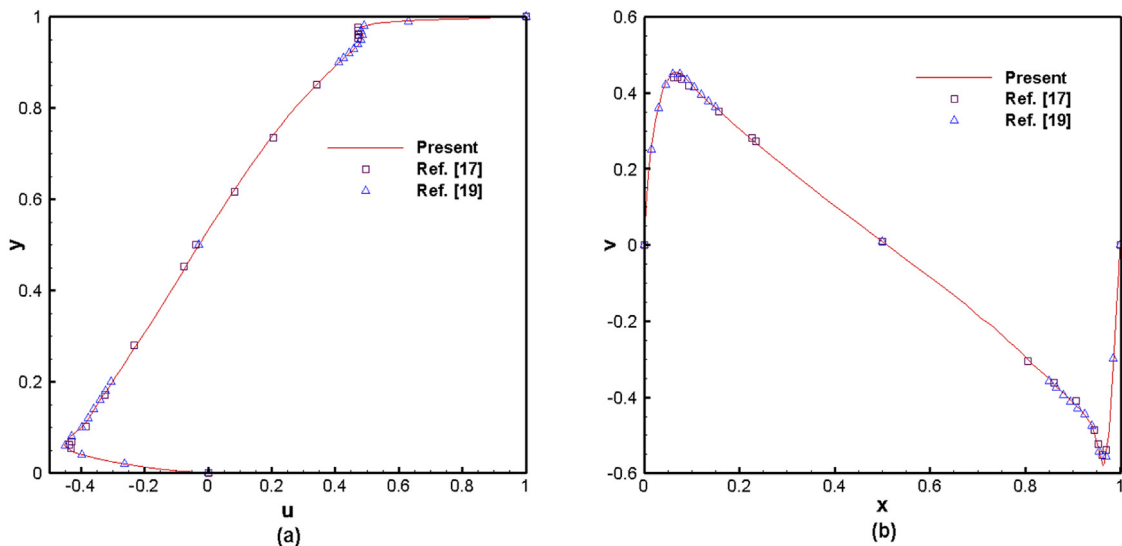

Fig. 10. (a) u-velocity profile on centreline CL_1 and (b) v-velocity profile on centreline CL_2 in a square cavity for $Re = 7500$.

Table 2
Comparison of vortex locations in a square cavity for $Re = 1000$ and 7500.

		Present		Ref. [25]		Ref. [27]	
		x	y	x	y	x	y
1000	Primary	0.5300	0.5650	0.5313	0.5625	0.5300	0.5650
	BL1	0.0825	0.0775	0.0859	0.0781	0.0833	0.0783
	BR1	0.8650	0.1125	0.8594	0.1094	0.8633	0.1117
	BL2	—	—	—	—	0.0050	0.0050
	BR2	0.9915	0.0060	0.9922	0.0078	0.9917	0.0067
7500	Primary	0.5125	0.5325	0.5117	0.5322	0.5133	0.5317
	BL1	0.0650	0.1525	0.0645	0.1504	0.0650	0.1517
	BR1	0.7900	0.0650	0.7813	0.0625	0.7900	0.0650
	TL1	0.0665	0.9125	0.0664	0.9141	0.0667	0.9133
	BL2	0.0115	0.0115	0.0117	0.0117	0.0117	0.0117
	BR2	0.9500	0.0420	0.9492	0.0430	0.9517	0.0417

Table 3
Percentage difference of u-velocity on centreline CL_1 with benchmark solution.

y	Present	Ref. [29]	Deviation (%)
	65×65	1024×1024	
0.9688	0.5800	0.5803	−0.0456
0.9531	0.4711	0.4724	−0.2770
0.7344	0.1877	0.1886	−0.4820
0.5000	−0.0618	−0.0621	−0.4691
0.2813	−0.2792	−0.2804	−0.4141
0.1016	−0.2993	−0.3003	−0.3401
0.0625	−0.2015	−0.2023	−0.4151

Table 4
Percentage difference of v-velocity on centreline CL_2 with benchmark solution.

x	Present	Ref. [29]	Deviation (%)
	65×65	1024×1024	
0.9609	−0.2927	−0.2933	−0.1976
0.9453	−0.4090	−0.4102	−0.2912
0.8594	−0.4257	−0.4263	−0.1436
0.5000	0.0257	0.0258	−0.3660
0.2266	0.3329	0.3340	−0.3404
0.0938	0.3319	0.3329	−0.2894
0.0703	0.2953	0.2962	−0.2873

$= 1000$ from the velocity data of Bruneau and Saad [29] using a high resolution grid of 1024×1024 to quantitatively verify the accuracy of the segregated SEM. It can be seen that there is a remarkable agreement between the present and the reference values with a maximum difference of less than 0.5%, even if only 65×65 nodes are used in the current calculation.

For flow of $Re \geq 7500$, a linear stability analysis [29,30] shows that the steady-state solution will gradually lose its stability to transform into a periodic solution, which corresponds to the first Hopf bifurcation. However, steady-state solutions are claimed in some publications [27,31,32] to exist for $Re = 10000$ or even higher Reynolds numbers. Therefore the segregated SEM is applied to the flow of $Re = 10000$ to explore the flow phenomena. The time evolution of the u-velocity at the monitoring point (0.8643, 0.1357) is plotted in Fig. 11(a) and a Fourier analysis is performed for this signal. The power spectrum, as well as the phase trajectory, in Fig. 11(b) and (c) demonstrates that the solution is not a purely periodic one, but has a dominant harmonic and a subharmonic. A sequence of six streamline contours at discrete time intervals for a cycle of $T = 2.0$ is illustrated in Fig. 12. It is seen that the streamline pattern is repeated after a period. The main structure in the cavity is invariant in addition to the periodic changes of small eddies in the corner, which verify the result of the power spectrum. From the above results, it can be deduced that there is a critical Reynolds number and that the steady-state flow will be replaced by an almost periodic one when Re is beyond the threshold value.

4.2.2. Results for the flow in an inclined cavity

Two different inclination angles of $\theta = \pi/3$ and $\theta = \pi/4$ are considered in this context. Figs. 13 and 14 show the steady-state streamline contours in the inclined cavities for the two angles, respectively, for the cases of $Re = 1000$ and 5000. With the increase of the Reynolds number, the primary vortex moves towards the downstream end of the lid and it becomes smaller and smaller while the secondary vortex gradually expands. When the inclination angle θ is reduced from $\pi/3$ to $\pi/4$, the primary vortex reaches the right side of the cavity for $Re = 5000$, which demonstrates that the change in geometry makes the flow inside the cavity more intense.
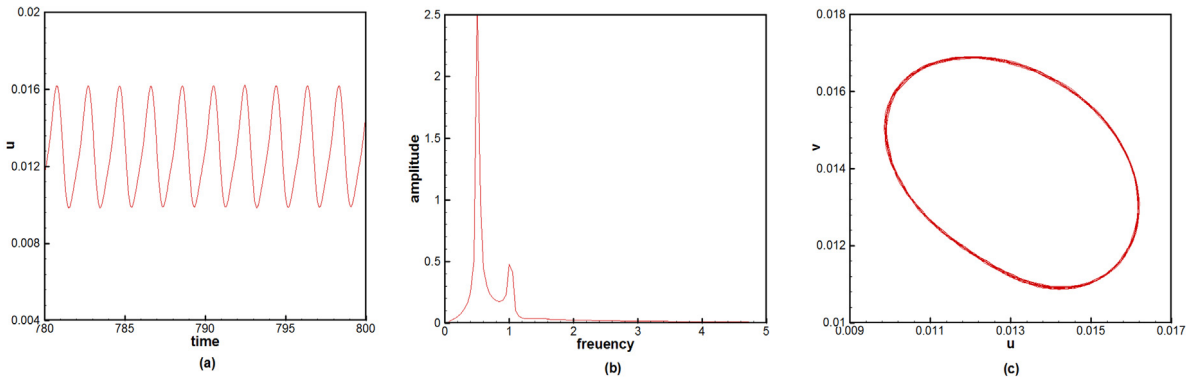
Fig. 11. (a) Horizontal velocity history, (b) Power spectrum and (c) Phase trajectory at monitoring point (0.8643, 0.1357) in a square cavity for $Re = 10000$.
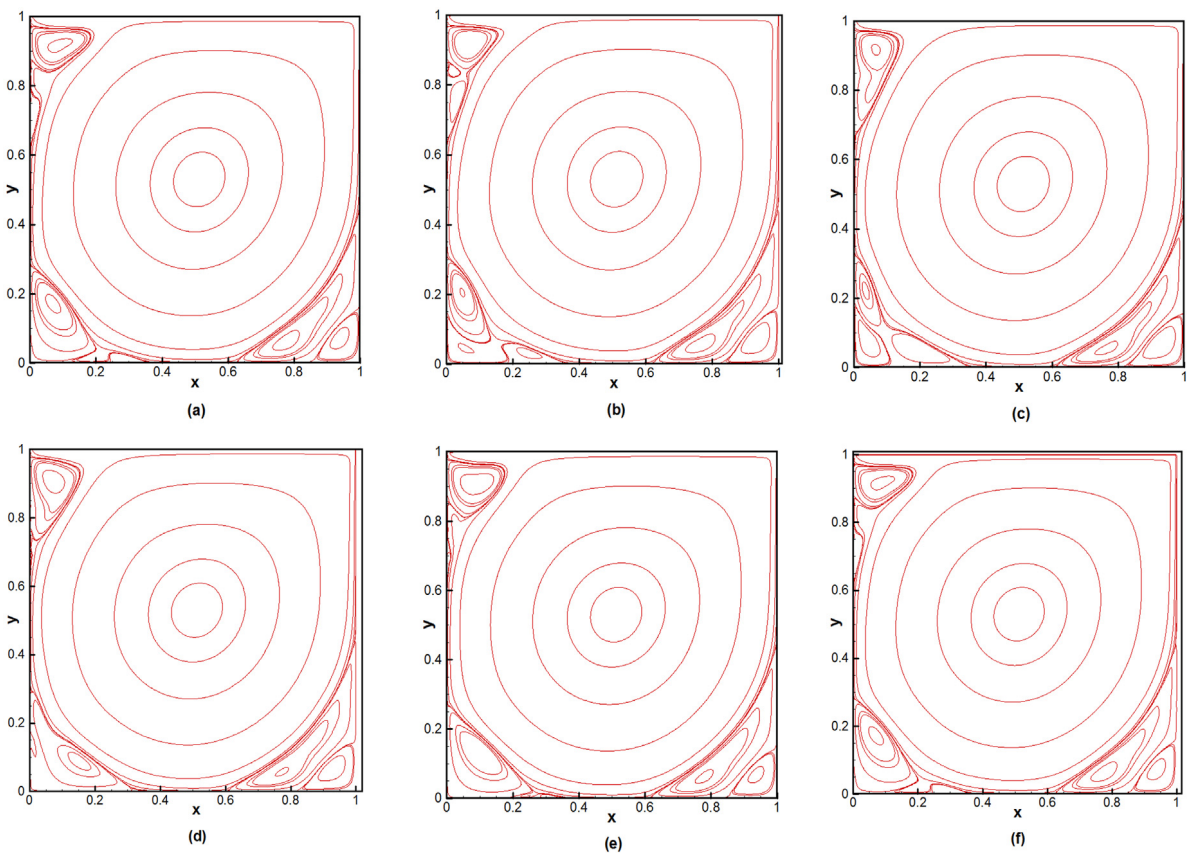

Fig. 12. Evolution of streamlines during one time period in a square cavity for $Re = 10000$ (a) $t = 0T$, (b) $t = 0.4T$, (c) $t = 0.8T$, (d) $t = 1.2T$, (e) $t = 1.6T$ and (f) $t = 2.0T$.

In Fig. 15, the velocity profiles on the centrelines CL_1 and CL_2 in the cavity with $\theta = \pi/4$ for $Re = 1000$ are compared with the benchmark solutions of Demirdžić et al. [26] obtained on a grid of 320×320. It is clear that the numerical results are in agreement with the reference ones.

4.3. Flow over a backward-facing step

The segregated SEM is next applied to the well-known problem of flow over a backward-facing step in a channel. This example has been extensively studied by many researchers [33–35] both numerically and experimentally, and it is an
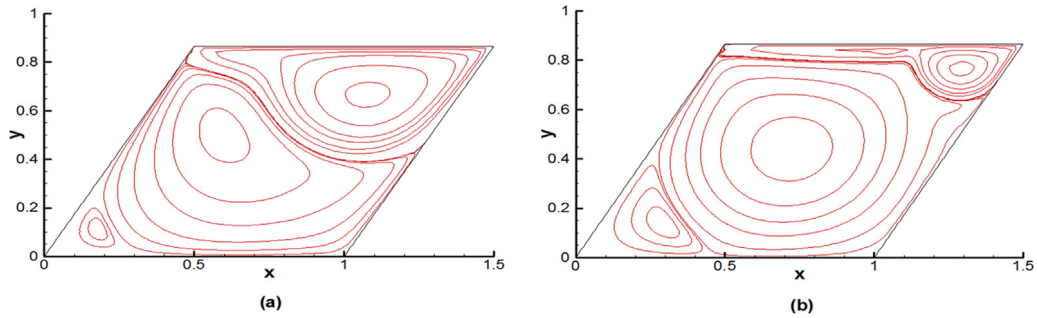
Fig. 13. Streamline contours in an inclined cavity with $\theta = \pi/3$ for (a) $Re = 1000$ and (b) $Re = 5000$.
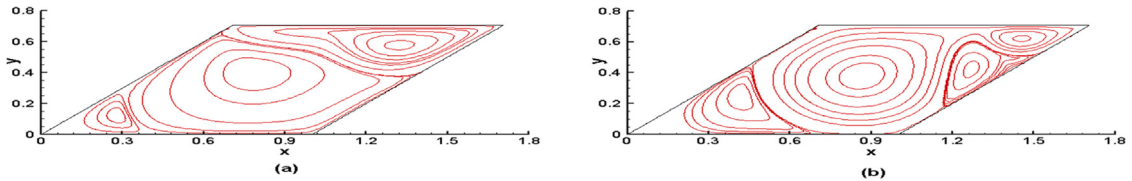

Fig. 14. Streamline contours in an inclined cavity with $\theta = \pi/4$ for (a) $Re = 1000$ and (b) $Re = 5000$.
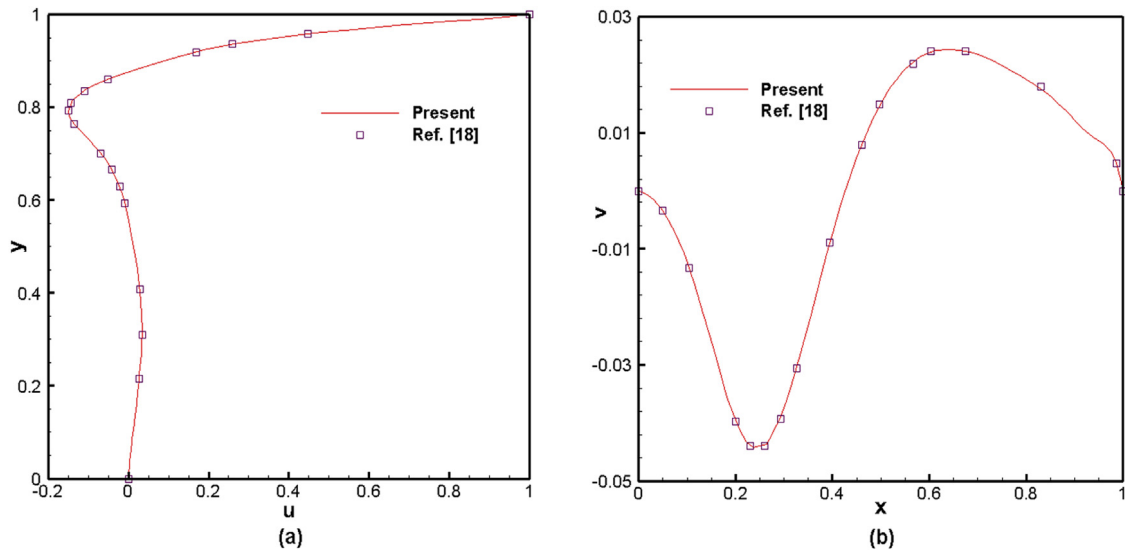

Fig. 15. (a) u-velocity profile on centreline CL_1 and (b) v-velocity profile on centreline CL_2 in an inclined cavity with $\theta = \pi/4$ for $Re = 1000$.

excellent test case for the validity and accuracy of the present numerical scheme. The problem configuration is presented in Fig. 16. The geometry is set to be the same as that used by Armaly et al. [33]. A Poiseuille parabolic profile $u = 6y - 6y^2$, $v = 0$ is prescribed at the inflow with a mean velocity of 1.0, the no-slip boundary condition is employed for the solid walls at the top and bottom sides. At the outlet, the velocity boundary is derived from the assumption of full development and the law of mass conservation, which can be expressed as

$$u = \frac{6}{(1+S)^3}[S + (1-S)y - y^2], v = 0 \tag{41}$$

where S is the height of the step and $S = 0.9403$. The Reynolds number is defined with the characteristic velocity u_0 equal to the mean value of the inflow velocity and with the characteristic length L_0 equal to the upstream channel height. Three different element divisions (10×4, 14×4 and 16×6) with an eighth-order polynomial in each element are employed to test the grid independence for the expansion section of the channel. Numerical experiments using the three nonuniform grids of 81×33, 113×33 and 129×49 are performed for the flow of $Re = 100$, and the u-velocities on the vertical line
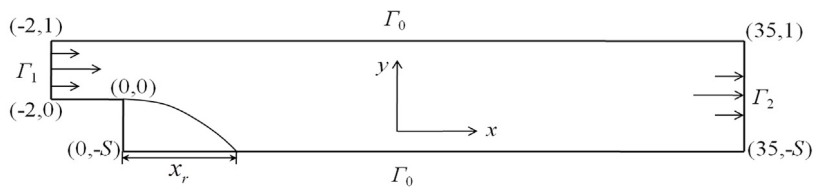
Fig. 16. Schematic and boundary conditions for the flow over a backward-facing step in a channel.
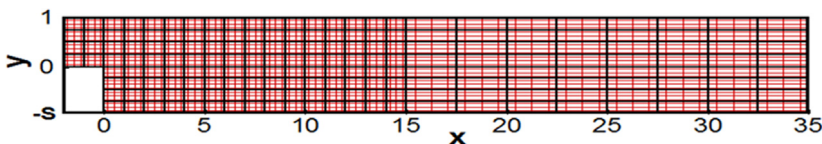

Fig. 17. Nonuniform grid used for the flow over a backward-facing step in a channel.

Table 5
Grid independence test of u-velocity on vertical line at $x = 7.76$ in a channel.

y	81×33	113×33	129×49
−0.8449	0.1732	0.1476	0.1475
−0.7656	0.2941	0.2569	0.2563
−0.6093	0.4764	0.4439	0.4432
0.0000	0.8326	0.7847	0.7841
0.6429	0.4748	0.4437	0.4432
0.7857	0.3417	0.2875	0.2871
0.8571	0.2134	0.1990	0.1988

at $x = 7.76$ are presented in Table 5. It can be seen that the grid of 113×33 shown in Fig. 17 is sufficient to compute the flow. The time step $\Delta t = 0.01$ and the under-relaxation factors $\alpha_u = 0.7$ and $\alpha_p = 0.2$ are also adopted in the simulation.

The steady-state streamline contours for $Re = 100, 200, 500$ and 600 are presented in Fig. 18. It is observed that a vortex exists in the re-circulation zone behind the step and the reattachment length x_r continually increases when Re becomes larger. It can also be noticed that a secondary vortex appears on the upper wall for $Re = 500$. The reattachment length versus the Reynolds number is compared with the experimental and numerical results of Armaly et al. [33] as shown in Fig. 19. The present computed results are in better agreement with the experimental data than with the numerical results for the flow of $Re \leq 600$. Meanwhile, the present value apparently deviates from the experimental one for $Re = 800$. It is mainly because the three-dimensional nature of the flow is already obvious as the Reynolds number reaches 800 and the assumption of full development used for the outlet boundary condition no longer holds. The velocity profiles on the vertical lines at different x-positions for $Re = 100$ and 389 are shown in Fig. 20. It can be seen that the present velocity values are consistent with the experimental data of Armaly et al. [33].

5. Conclusions

In this paper an efficient high-order velocity–pressure formulation that combines the SEM and the SIMPLEST algorithm is presented for the two-dimensional transient Navier–Stokes equations.

The accuracy of the scheme is demonstrated by the test problem with an analytical solution. Higher accuracy and faster convergence can be obtained when high-order polynomials in each element are employed. Additionally, the scheme is applied to flow in a lid-driven cavity and flow over a backward-facing step. The steady-state solution of the flow in a lid-driven square cavity for $Re = 7500$ and the steady-state solution of the flow in a lid-driven inclined cavity for $Re = 5000$ are obtained, respectively. Despite the fact that fewer nodal points are used in the simulation, the computed results are in excellent agreement with the benchmark solutions obtained on high resolution grids. For the flow over a backward-facing step for $Re \leq 600$, the present results also compare very well with the experimental results. The ability of the scheme is further highlighted by capturing the almost periodic solution for the flow for $Re = 10000$ in a lid-driven square cavity.

Based on the numerical experiments, we believe that the separation of velocity and pressure and the spectral accuracy make the segregated SEM an efficient and accurate approach and have the potential to be further applied to more complicated incompressible flow problems in the future.

Declaration of competing interest

The authors declare that they have no known competing financial interests or personal relationships that could have appeared to influence the work reported in this paper.
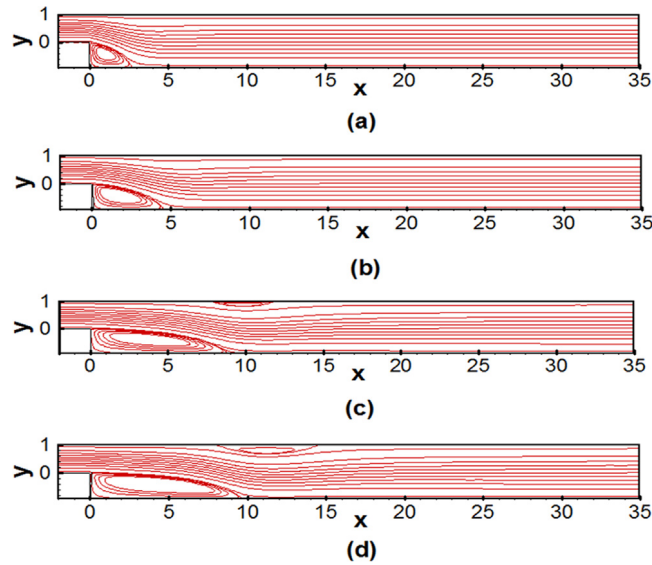
Fig. 18. Streamline contours of the flow over a backward-facing step for (a) $Re = 100$, (b) $Re = 200$, (c) $Re = 500$ and (d) $Re = 600$.
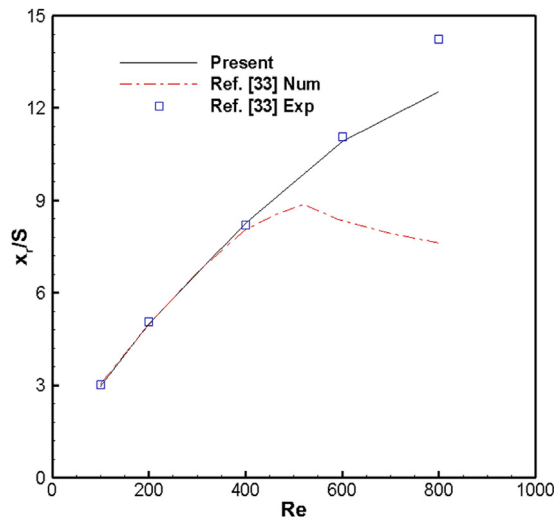

Fig. 19. Reattachment length plotted as a function versus the Reynolds number.

Acknowledgement

Appendix

For each iteration in a time step of the SIMPLE algorithm, the decoupling of velocity and pressure is equivalent to the process expressed by the following equations

$$\begin{cases} \dfrac{\boldsymbol{u}^{k+1,*} - \boldsymbol{u}^n}{\Delta t} + B(\dfrac{\boldsymbol{u}^{k+1,*} + \boldsymbol{u}^n}{2}, \dfrac{\boldsymbol{u}^{k+1,*} + \boldsymbol{u}^n}{2}) - \nu\Delta(\dfrac{\boldsymbol{u}^{k+1,*} + \boldsymbol{u}^n}{2}) + \nabla p^k = \boldsymbol{f}^{n+\frac{1}{2}} \\ \boldsymbol{u}^{k+1,*} + \boldsymbol{u}^n = 0, \text{ on } \Gamma \end{cases} \tag{A.1}$$

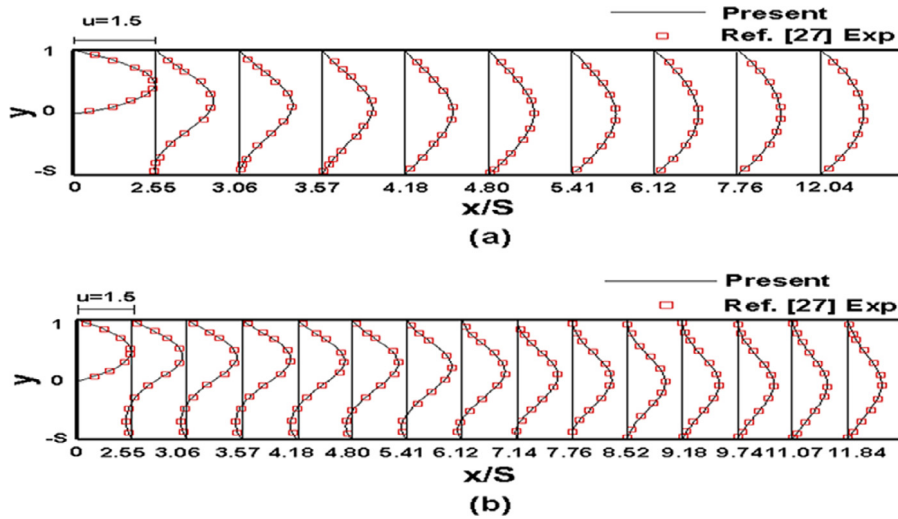$$\boldsymbol{u}^{k+1} = \boldsymbol{u}^{k+1,*} - \frac{1}{2}\Delta t(p^{k+1} - p^k) \tag{A.2}$$

Fig. 20. Streamwise velocity profiles at various streamwise locations for (a) $Re = 100$ and (b) $Re = 389$.

$$\begin{cases} \nabla \cdot \boldsymbol{u}^{k+1} = 0 \\ \boldsymbol{u}^{k+1} \cdot \boldsymbol{n} = 0, \ \text{on } \Gamma \end{cases} \tag{A.3}$$

where Δt is the time step, $B(\boldsymbol{u}, \boldsymbol{v}) = \boldsymbol{u} \cdot \nabla \boldsymbol{v}$. As in the mainbody, the time step superscript $n + 1$ of intermediate values in the iterative process is omitted, and $\boldsymbol{u}^{k+1,*}$ is the intermediate velocity for the $(k + 1)$th iterative step of the $(n + 1)$th time step. The velocity field and source term of the $(n + \frac{1}{2})$th time step are adopted to discretize (A.1), which can be considered as looking for the numerical solution of this time step. Although there are small differences between the above discrete form and the one adopted in the mainbody, the decoupling method of velocity and pressure employed by the two is exactly the same.

Let P be the projector in $L^2(\Omega)$ onto the divergence-free subspace $\boldsymbol{u}^{k+1} = P\boldsymbol{u}^{k+1,*}$. Adding (A.1) of the $(k + 1)$th iterative step and (A.2) of the kth iterative step, (A.1) can be rewritten as

$$\begin{cases} \dfrac{\boldsymbol{u}^{k+1,*} - \boldsymbol{u}^{n,*}}{\Delta t} + B\left(\dfrac{\boldsymbol{u}^{k+1,*} + P\boldsymbol{u}^{n,*}}{2}, \dfrac{\boldsymbol{u}^{k+1,*} + P\boldsymbol{u}^{n,*}}{2}\right) - \nu\Delta\left(\dfrac{\boldsymbol{u}^{k+1,*} + P\boldsymbol{u}^{n,*}}{2}\right) + \dfrac{1}{2}\nabla(3p^k - p^{k-1}) = \boldsymbol{f}^{n+\frac{1}{2}} \\ \boldsymbol{u}^{k+1,*} + P\boldsymbol{u}^n = 0, \ \text{on } \Gamma \end{cases} \tag{A.4}$$

$(\cdot, \cdot)$ is used to represent the scalar product in $L^2(\Omega)$. The dual space of $H_0^1(\Omega)$ is denoted by $H^{-1}(\Omega)$ and the duality between them is denoted by $\langle \cdot, \cdot \rangle$. The operator for the nonlinear term is defined as $b(\boldsymbol{u}, \boldsymbol{v}, \boldsymbol{w}) = (B(\boldsymbol{u}, \boldsymbol{v}), \boldsymbol{w})$, we note that $b(\boldsymbol{u}, \boldsymbol{v}, \boldsymbol{v}) = 0, \forall \boldsymbol{u} \in H, \forall \boldsymbol{v} \in H_0^1(\Omega)$. Taking the inner product of (A.4) with $\Delta t(\boldsymbol{u}^{k+1,*} + P\boldsymbol{u}^{n,*})$ and of (A.2) with $\frac{\Delta t}{2}(3p^k - p^{k-1})$, add the two formulae together, since $\nabla \cdot (P\boldsymbol{u}^{n,*}) = 0$, it can be obtained that

$$\begin{aligned} &(\boldsymbol{u}^{k+1,*} - \boldsymbol{u}^{n,*}, \boldsymbol{u}^{k+1,*} + P\boldsymbol{u}^{n,*}) + \dfrac{\nu\Delta t}{2}\left\|\nabla(\boldsymbol{u}^{k+1,*} + P\boldsymbol{u}^{n,*})\right\|^2 + \dfrac{\Delta t^2}{4}(\nabla(p^{k+1} - p^k), \nabla(3p^k - p^{k-1})) \\ &= \Delta t\langle \boldsymbol{u}^{k+1,*} - \boldsymbol{u}^{n,*}, \boldsymbol{f}^{n+1/2}\rangle \leq \dfrac{\nu\Delta t}{4}\left\|\nabla(\boldsymbol{u}^{k+1,*} + P\boldsymbol{u}^{n,*})\right\|^2 + C\Delta t\left\|\boldsymbol{f}^{n+1/2}\right\|_{-1}^2 \end{aligned} \tag{A.5}$$

where C is a genetic positive constant. We note that a Neumann pressure boundary condition is introduced into the continuity equation in the derivation of (A.5) to avoid the boundary influence on the analysis process. Making use of the analytical techniques in [24], we can infer that

$$\begin{aligned} (\boldsymbol{u}^{k+1,*} - \boldsymbol{u}^{n,*}, \boldsymbol{u}^{k+1,*} + P\boldsymbol{u}^{n,*}) &= \left\|\boldsymbol{u}^{k+1,*}\right\|^2 - \left\|\boldsymbol{u}^{n,*}\right\|^2 - \dfrac{\Delta t^2}{8}(\left\|\nabla(p^{k+1} - p^k)\right\|^2 \\ &- \left\|\nabla(p^k - p^{k-1})\right\|^2) + \dfrac{\Delta t^2}{8}\left\|\nabla(p^{k+1} - 2p^k + p^{k-1})\right\|^2 \end{aligned} \tag{A.6}$$

$$\begin{aligned} \dfrac{\Delta t^2}{4}(\nabla(p^{k+1} - p^k), \nabla(p^k - p^{k-1})) &= \dfrac{\Delta t^2}{4}(\left\|\nabla p^{k+1}\right\|^2 - \left\|\nabla p^k\right\|^2 - \left\|\nabla(p^{k+1} - p^k)\right\|^2) \\ &- \dfrac{\Delta t^2}{8}\left\|\nabla(p^{k+1} - 2p^k + p^{k-1})\right\|^2 + \dfrac{\Delta t^2}{8}(\left\|\nabla(p^{k+1} - p^k)\right\|^2 + \left\|\nabla(p^k - p^{k-1})\right\|^2) \end{aligned} \tag{A.7}$$

From (A.2), it can be obtained

$$\frac{\Delta t^2}{4} \left\| \nabla(p^{m+1} - p^m) \right\|^2 \leq \left\| \boldsymbol{u}^{m+1,*} \right\|^2 \tag{A.8}$$

Taking the sum of (A.5) for $k = 1$ to m, and utilizing the above inequalities, it is derived

$$\frac{\nu \Delta t}{4} \sum_{k=1}^{m} \left\| \nabla(\boldsymbol{u}^{k+1,*} + P\boldsymbol{u}^{n,*}) \right\|^2 + \frac{\Delta t^2}{8} \left\| \nabla p^{m+1} \right\|^2 \leq \left\| \boldsymbol{u}^1 \right\|^2 + \frac{\Delta t^2}{8} \left\| \nabla p^1 \right\|^2 + \| \boldsymbol{f} \|_{C([0,T];H^{-1})}^2 \tag{A.9}$$

Therefore, it can be seen that the decoupling scheme of velocity and pressure used in this paper is stable.

References

[1] S.V. Patankar, D.B. Spalding, A calculation procedure for heat, mass and momentum transfer in three-dimensional parabolic flows, Int. J. Heat Mass Transfer 15 (1972) 1787–1806.
[2] W.Q. Tao, Numerical Heat Transfer, second ed., Xi'an Jiaotong University Press, Xi'an, 2001.
[3] S.V. Patankar, A calculation procedure for two-dimensional elliptic situations, Numer. Heat Transfer 4 (1981) 409–425.
[4] J.P. Van Doormaal, G.D. Raithby, Enhancement of SIMPLE method for predicting incompressible fluid flows, Numer. Heat Transfer 7 (1984) 147–163.
[5] Z.G. Qu, W.Q. Tao, Y.L. He, Implementation of CLEAR algorithm on collocated grid system and application examples, Numer. Heat Transfer B 46 (2005) 65–96.
[6] D.L. Sun, W.Q. Tau, Z.G. Qu, An efficient segregated algorithm for incompressible fluid flow and heat transfer problems-IDEAL (inner doubly-iterative efficient algorithm for linked-equations) part I: mathematical formulation and solution procedure, Numer. Heat Transfer B 53 (2008) 1–17.
[7] D.L. Sun, W.Q. Tau, Z.G. Qu, An efficient segregated algorithm for incompressible fluid flow and heat transfer problems-IDEAL (inner doubly-iterative efficient algorithm for linked-equations) part II: application examples, Numer. Heat Transfer B 53 (2008) 18–38.
[8] J.G. Rice, R.J. Schnipke, An equal-order velocity-pressure formulation that does not exhibit spurious pressure modes, Comput. Methods Appl. Mech. 58 (1986) 135–149.
[9] G.P.A.G. van Zijl, C.G. du Toit, A SIMPLEST finite element solution of the incompressible Navier–Stokes equations, in: Proceedings of the Symposium on Finite Element Method, 1992.
[10] C.G. du Toit, A segregated finite element solution for non-isothermal flow, Comput. Methods Appl. Mech. 182 (2000) 457–481.
[11] A. Malatip, N. Wansophark, P. Dechaumphai, Combined streamline upwind Petrov Galerkin method and segregated finite element algorithm for conjugate heat transfer problems, J. Mech. Sci. Technol. 20 (10) (2006) 1741–1752.
[12] A.T. Patera, A spectral element method for fluid dynamics: Laminar flow in a channel expansion, J. Comput. Phys. 54 (1984) 468–488.
[13] C.J. Xu, Y.M. Lin, Analysis of iterative methods for the viscous/inviscid coupled problem via a spectral element approximation, Int. J. Number. Meth. Fluids 32 (2000) 619–646.
[14] H.J. Kim, A. Beskok, An algebraic factorisation scheme for spectral element solution of incompressible flow and scalar transport, Int. J. Comput. Fluid Dyn. 24 (3–4) (2010) 95–108.
[15] R. Ranjan, A.T. Chronopoulos, Y.S. Feng, Computational algorithms for solving spectral/ hp stabilized incompressible flow problems, J. Math. Res. 8 (2016) 21–39.
[16] L.C. Hsu, C.L. Chen, J.Z. Ye, A study of flow patterns for staggered cylinders at low reynolds numbers by spectral element method, J. Mech. Sci. Technol. 31 (6) (2017) 2765–2780.
[17] L.Z. Chen, J. Shen, C.J. Xu, L.S. Luo, Parallel spectral-element direction splitting method for incompressible Navier–Stokes equations, Appl. Numer. Math. 84 (2014) 66–79.
[18] B.E. Merrill, Y.T. Peet, P.F. Fischer, J.W. Lottes, A spectrally accurate method for overlapping grid solution of incompressible Navier–Stokes equations, J. Comput. Phys. 307 (2016) 60–93.
[19] A. Bolis, C.D. Cantwell, D. Moxey, D. Serson, S.J. Sherwin, An adaptable parallel algorithm for the direct numerical simulation of incompressible turbulent flows using a Fourier spectral/ hp element method and MPI virtual topologies, Comput. Phys. Comm. 206 (2016) 17–25.
[20] D. Serson, J.R. Meneghini, S.J. Sherwin, Direct numerical simulation of the flow around wings with spanwise at a very low Reynolds number, Comput. Fluids 146 (2017) 117–124.
[21] Y.Y. Hu, J. Xie, W. Zhang, Solution of two dimensional incompressible Navier–Stokes equation by parallel spectral finite element method, J. Comput. Appl. 37 (1) (2017) 42–47.
[22] S. Mohapatra, S. Ganesan, A non-conforming least squares spectral element formulation for oseen equations with applications to Navier–Stokes equations, Numer. Funct. Anal. Optim. 37 (10) (2016) 1295–1311.
[23] J.L. Guermond, P. Minev, J. Shen, An overview of projection methods for incompressible flows, Comput. Methods Appl. Mech. Engrg. 195 (2006) 6011–6045.
[24] J. Shen, On error estimates of the projection methods for the Navier–Stokes equations: second-order schemes, Math. Comp. 65 (215) (1996) 1039–1065.
[25] U. Ghia, N. Ghia, C.T. Shin, High- re solutions for incompressible flow using the Navier–Stokes equations and a multigrid method, J. Comput. Phys. 48 (1982) 387–411.
[26] I. Demirdžić, Ž. Lilek, M. Perić, Fluid flow and heat transfer test problems for non-orthogonal grids: bench-mark solutions, Int. J. Numer. Methods Fluids 15 (1992) 329–354.
[27] E. Erturk, T.C. Corke, C. Gökcöl, Numerical solution of 2-D steady incompressible driven cavity flow at high Reynolds numbers, Int. J. Numer. Methods Fluids 48 (2005) 747–774.
[28] D.S. Kuma, A.K. Dass, A. Dewan, A multigrid-accelerated code on graded Cartesian meshes for 2D time-dependent incompressible viscous flows, Eng. Appl. Comput. Fluids 4 (1) (2010) 71–90.
[29] C.H. Bruneau, M. Saad, The 2D lid-driven cavity problem revisited, Comput. Fluids 35 (2006) 326–348.
[30] Y.F. Peng, Y.H. Shiau, R.R. Hwang, Transition in a 2-D lid-driven cavity flow, Comput. Fluids 32 (2003) 337–352.
[31] E. Barragy, G.F. Carey, Stream function-vorticity driven cavity solution using p finite elements, Comput. Fluids 26 (5) (1997) 453–468.
[32] E. Erturk, Discussions on driven cavity flow, Int. J. Numer. Methods Fluids 60 (2009) 275–294.
[33] B.F. Armaly, F. Durst, J.C.F. Pereira, B. Schönung, Experimental and theoretical investigation of backward-facing step flow, J. Fluid Mech. 127 (1983) 473–496.
[34] J. Kim, P. Moin, Application of a fractional-step method to incompressible Navier–Stokes equations, J. Comput. Phys. 59 (1985) 308–323.
[35] D.K. Gartling, A test problem for outflow boundary conditions—flow over a backward-facing step, Int. J. Numer. Methods Fluids 11 (1990) 953–967.